

INFORMATION TO USERS

This reproduction was made from a copy of a document sent to us for microfilming. While the most advanced technology has been used to photograph and reproduce this document, the quality of the reproduction is heavily dependent upon the quality of the material submitted.

The following explanation of techniques is provided to help clarify markings or notations which may appear on this reproduction.

1. The sign or "target" for pages apparently lacking from the document photographed is "Missing Page(s)". If it was possible to obtain the missing page(s) or section, they are spliced into the film along with adjacent pages. This may have necessitated cutting through an image and duplicating adjacent pages to assure complete continuity.
2. When an image on the film is obliterated with a round black mark, it is an indication of either blurred copy because of movement during exposure, duplicate copy, or copyrighted materials that should not have been filmed. For blurred pages, a good image of the page can be found in the adjacent frame. If copyrighted materials were deleted, a target note will appear listing the pages in the adjacent frame.
3. When a map, drawing or chart, etc., is part of the material being photographed, a definite method of "sectioning" the material has been followed. It is customary to begin filming at the upper left hand corner of a large sheet and to continue from left to right in equal sections with small overlaps. If necessary, sectioning is continued again—beginning below the first row and continuing on until complete.
4. For illustrations that cannot be satisfactorily reproduced by xerographic means, photographic prints can be purchased at additional cost and inserted into your xerographic copy. These prints are available upon request from the Dissertations Customer Services Department.
5. Some pages in any document may have indistinct print. In all cases the best available copy has been filmed.

**University
Microfilms
International**

300 N. Zeeb Road
Ann Arbor, MI 48106

1327020

Yang, Hsien-Min

PRINCIPAL COMPONENTS AND TEXTURE ANALYSIS OF THE NS-001
THEMATIC MAPPER SIMULATOR DATA IN THE ROSEMONT MINING
DISTRICT, ARIZONA

The University of Arizona

M.S. 1985

**University
Microfilms
International** 300 N. Zeeb Road, Ann Arbor, MI 48106

PLEASE NOTE:

In all cases this material has been filmed in the best possible way from the available copy. Problems encountered with this document have been identified here with a check mark .

1. Glossy photographs or pages
2. Colored illustrations, paper or print
3. Photographs with dark background
4. Illustrations are poor copy
5. Pages with black marks, not original copy
6. Print shows through as there is text on both sides of page
7. Indistinct, broken or small print on several pages
8. Print exceeds margin requirements
9. Tightly bound copy with print lost in spine
10. Computer printout pages with indistinct print
11. Page(s) _____ lacking when material received, and not available from school or author.
12. Page(s) _____ seem to be missing in numbering only as text follows.
13. Two pages numbered _____. Text follows.
14. Curling and wrinkled pages
15. Dissertation contains pages with print at a slant, filmed as received
16. Other _____

University
Microfilms
International

PRINCIPAL COMPONENTS AND TEXTURE ANALYSIS OF THE NS-001
THEMATIC MAPPER SIMULATOR DATA IN THE ROSEMONT MINING
DISTRICT, ARIZONA

by
Hsien-Min Yang

A Thesis Submitted to the Faculty of the
DEPARTMENT OF MINING AND GEOLOGICAL ENGINEERING
In Partial Fulfillment of the Requirements
For the Degree of
MASTER OF SCIENCE
WITH A MAJOR IN GEOLOGICAL ENGINEERING
In the Graduate College
THE UNIVERSITY OF ARIZONA

1 9 8 5

STATEMENT BY AUTHOR

This thesis has been submitted in partial fulfillment of requirements for an advanced degree at The University of Arizona and is deposited in the University Library to be made available to borrowers under rules of the Library.

Brief quotations from this thesis are allowable without special permission, provided that accurate acknowledgment of source is made. Requests for permission for extended quotation from or reproduction of this manuscript in whole or in part may be granted by the head of the major department or the Dean of the Graduate College when in his or her judgement the proposed use of the material is in the interests of scholarship. In all other instances, however, permission must be obtained from the author.

SIGNED: Asien-Min Yang

APPROVAL BY THESIS DIRECTOR

This thesis has been approved on the date shown below:

Charles E. Glass
C. E. GLASS
Professor of Geological
Engineering

OCT. 29, 1985
DATE

ACKNOWLEDGMENTS

I would like to express my sincerest gratitude to Dr. Charles E. Glass, the thesis advisor, for his encouragement, guidance, and support throughout this study. He first gave me the opportunity to explore the areas of geologic remote sensing and digital image processing.

Applications of the co-occurrence matrix algorithm in the study would not have been possible without the assistance of Dr. R. A. Schowengerdt, who served on the thesis committee. He is also thanked for allowing the use of his computer programs for the texture analysis.

I also wish to thank Dr. Jaak J. K. Daemen, who encouraged me and served on the thesis committee.

Sincere appreciation is extended to my parents and my wife for their moral and financial support throughout my academic career.

TABLE OF CONTENTS

	Page
LIST OF ILLUSTRATIONS	v
LIST OF TABLES	ix
ABSTRACT	x
1. INTRODUCTION	1
2. GEOLOGY OF THE ROSEMONT MINING DISTRICT	8
Stratigraphy	8
Igneous Rocks	10
Structural Geology	10
3. ANALYSIS OF REMOTE-SENSING DATA	16
Thematic Mapper Simulator Data	16
Facilities and Software Available	16
Analysis of the TMS Data Structure in the study area	17
4. PRINCIPAL COMPONENTS ANALYSIS	22
5. TEXTURE ANALYSIS	31
Gradient Operator	31
Co-occurrence Matrix	32
Textural Transformation	36
6. RESULTS AND DISCUSSION	46
Principal Component Images	46
Texture Features	60
7. CONCLUSIONS	72
REFERENCES	76

LIST OF ILLUSTRATIONS

Figure	Page
1.1a A high texture content region defined by the red line in the original image	6
1.1b The gray level profile along the red line in Fig. 1.1a	6
1.1c A low texture content region defined by the red line in the original image	7
1.1d The gray level profile along the red line in Fig. 1.1c	7
2.1 Location map of the Rosemont mining district	13
2.2 Generalized geologic map of the Rosemont mining district	14
2.3 Stratigraphy column of the Rosemont district	15
3.1a Scattergram of the two TMS visible bands having the highest correlation (0.965 between bands 2 and 3)	21
3.1b Scattergram of the visible and the near infrared bands having the lowest correlation (0.730 between bands 1 and 7)	21
4.1 Rotation and shift of the coordinate axes in two dimensions	27
4.2 Two dimensional correlation diagrams	28
4.3 Eigenvectors and eigenvalues in two dimensions	29

LIST OF ILLUSTRATIONS--Continued

Figure		Page
5.1a	Convolution kernels used to construct a first derivative image enhancing the vertical direction linear features	39
5.1b	A first derivative image enhancing horizontal direction linear features	39
5.2	Four independent angles (separation vectors) for $D = 1$	40
5.3a	A 4 by 4 image with 4 gray levels	41
5.3b	Location in the co-occurrence matrix	41
5.3c	Co-occurrence matrices at four different angles	41
5.4	Moving window algorithm. Gray levels of pixels within a window are used to measure a specified texture feature	42
5.5a	Parameters defining the COM in this experiment. Dimension of the COM	43
5.5b	Spatial window size (3 by 3)	43
5.5c	Parameters defining the COM in this experiment. Distance ($D = 1$)	44
5.5d	Angle ($A = 0^\circ, 45^\circ, 90^\circ, -45^\circ$)	44
6.1a	Unenhanced original TMS images of the study area. Band 3 (0.63-0.69 μm)	53
6.1b	Band 4 (0.79-0.90 μm)	53
6.1c	Unenhanced original TMS images of the study area. Band 6 (1.55-1.75 μm)	54
6.1d	Band 7 (2.08-2.36 μm)	54
6.2a	TMS (4-band data) principal component images of the Rosemont mining district, Arizona. PC1, a weighted average image.	55

LIST OF ILLUSTRATIONS--Continued

Figure	Page
6.2b PC2. G = granodiorite, M = Greaterville intrusives, H = Helvetia intrusives, Q = Bolsa Quartzite, L = sedimentary rocks mainly limestone	55
6.2c TMS (4-band data) principal component images of the Rosemont mining district, Arizona. PC3. A = Altered Cretaceous rocks, L = Paleozoic sedimentary rocks mainly limestone, H = Helvetia intrusives	56
6.2d PC4, having the most noise	56
6.3a Color composite of the first three principal components (PC1 in blue, PC2 in green, and PC3 in red).	57
6.3b Color composite of PC2, PC3, and PC4. (PC2 in blue, PC3 in green, and PC4 in red).	58
6.3c Color composite of the original TMS bands (band 4 in red, band 6 in green, band 7 in blue).	59
6.4a Gradient images derived from the first principal component image. Gradient image enhancing linear features in the vertical direction	66
6.4b Gradient image enhancing linear features in the horizontal direction	66
6.4c Gradient images derived from the first principal component image. Gradient magnitude image enhancing all directional linear features	67
6.5a Co-occurrence matrix features. Angular Second Moment (ASM) image	68
6.5b Contrast (CON) image	68
6.6a Textural transformation features. Negatively transformed Standard Deviation image (STD) with a 3 by 3 window	69

LIST OF ILLUSTRATION--Continued

Figure		Page
6.6b	Negatively transformed Mean of Squared Length Differences image (MSQ) with a 3 by 3 window.	69
6.6c	Textural transformation features. Negatively transformed Range image (RAN) with a 3 by 3 window	70
6.6d	Negatively transformed Range image (RAN) with a 5 by 5 window	70
6.6e	Textural transformation features. A pseudocolored version of the Range image (RAN) with a 3 by 3 window	71

LIST OF TABLES

Table		Page
3.1	Characteristics of two remote sensing systems	19
3.2	Statistical parameters of the probability density function of gray levels in the original NS-001 channels of the Rosemont mining subimage	20
3.3	Correlation matrix of the original NS-001 channels of the Rosemont mining subimage . . .	20
4.1	Weights for Eigenvectors	30
5.1	Computation time for the co-occurrence matrix features with different image sizes . .	45

ABSTRACT

Multispectral Visible-Near Infrared (VNIR) data were acquired with an aerial scanner over the Rosemont mining district of Arizona. The scanner was designed to simulate the Landsat-4 Thematic Mapper (TM) scanner.

Geologic information on digital images usually consists of two forms, spectral and textural. The principal components technique was chosen to enhance the spectral information. This technique enhances tone information resulting from variations in the reflectance of different lithologic units within different spectral bands.

Gradient images are used to enhance geologic structural information. The co-occurrence matrix and textural transformation are evaluated as an automated linear-features mapping tool; they automatically delineate textures which may reflect geologic structures, drainage density, or drainage patterns. The features derived from the co-occurrence matrix and textural transformation are similar; they are highly correlated. The textural transformation, however, is more practical from a computational point of view.

CHAPTER 1

INTRODUCTION

One of the principal roles of digital image processing for mineral exploration is to provide techniques for handling multispectral data. Both structural and lithologic information can be extracted from multispectral images. This information makes it possible to understand the geologic features in a digital image and to discriminate them with appropriate interpretation.

Image enhancement plays an important role in geologic remote sensing. In most cases, however, geologic information obtained from unprocessed multispectral images is limited because low contrast and spectral redundancy make regions of tonal variations in multispectral imagery difficult to discriminate. For this reason enhancement techniques such as contrast stretches, filters, ratios, principal components analysis etc. have been developed to enhance images. The techniques often provide significant information that can not be observed directly from unprocessed images.

Image classification, another important branch of digital image processing, provides useful applications in

the fields of agriculture, forestry, land use etc. Geologic thematic maps generated from image classification techniques, however, are often not sufficient to provide the detail needed for most geologic studies.

There are basically two types of information contained in an image: image tonal information and image textural information. Image tone refers to the brightness or darkness of a surface as represented by an image. Tone is a measure of the reflected or emitted electromagnetic energy from a surface detected in some portion of the electromagnetic spectrum. Tone is fundamental to image interpretation in all fields. The principal components (or Karhunen - Loeve) transformation (commonly used as a data compression technique) was used in this study as a technique to enhance image tonal (spectral) information, compress the image data, and reduce noise.

Image texture, which refers to the spatial frequency of tone changes throughout an image, can be defined by spatial relationships of tonal patterns in an image. In the thematic mapper simulator data depicting the study area (Rosemont mining district, Arizona), for example, image texture represents landforms and drainage patterns which have geologic significance. Areas having abrupt changes in gray levels are regarded as regions

having high texture content, whereas relatively homogeneous areas having subtle changes in gray levels are considered to have low texture content (Schowengerdt, 1981). Figure 1.1 depicts a region in the study area having a high degree of texture (Figure 1.1a and 1.1b) and an area having a low degree of texture (Figure 1.1c and 1.1d). Unlike image tonal information, however, image textural information is not routinely acquired by remote sensing instruments directly; it must be extracted. To use image texture as a digital image enhancement or classification technique requires a quantitative description of image texture content. Although texture is an important recognition element of digital image analysis, no formal mathematical approaches or precise definition have been accepted to provide quantitative texture information; quantitative texture measurements tend to be ad hoc.

Gradient operators, which are directional high pass filters, were selected for this study to enhance geologic structural information. Co-occurrence matrix and textural transformation, two examples of statistical algorithms (Haralick, 1979), were studied in this project to evaluate their ability to automatically delineate topographic lineaments associated with geologic structures and drainage patterns. The co-occurrence matrix algorithm was chosen

because it is one of the most commonly used statistical approaches. The computation cost needed to generate the second-order textural features, however, is high.

Therefore, a relatively simple algorithm, textural transformation, was also chosen to see if it can extract equivalent textural information in less computation time.

This study comprises two objectives. First, to determine if the principal components analysis is a useful technique for distinguishing lithologic units including surficial hydrothermal alteration zones in the study area. Second, to apply gradient operators and two statistical approaches (co-occurrence matrix and textural transformation) to the images to see if they can enhance or automatically delineate textures which may reflect geologic structures and drainage patterns in the study area. The aim is to determine if a combination of principal components analysis and texture analysis can contribute to geologic mapping.

Thematic mapper simulator (TMS) data, which have higher spatial, spectral, and radiometric resolution than the Landsat multispectral scanners (MSS) data, have previously proven to be useful for detailed geologic investigations (Abrams, 1983; Bailey, 1982). For this reason, remotely sensed data used in this study were

acquired with a Visible - Near Infrared (VNIR) scanner, NS-001, which simulates the Landsat - 4 Thematic Mapper (TM) scanner.

(a)



(b)

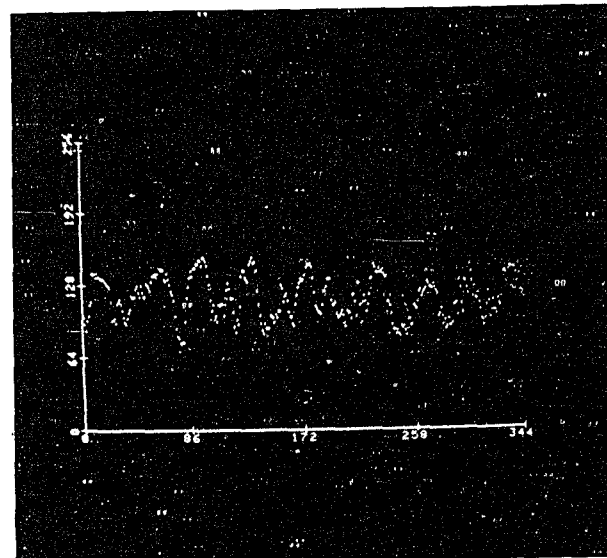


Figure 1.1. (a) A high texture content region defined by the red line in the original image. (b) The gray level profile along the red line in (a).

(c)



(d)

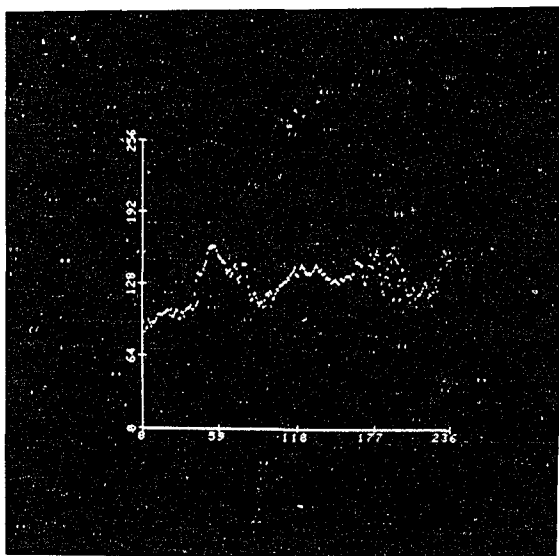


Figure 1.1. (c) A low texture content region defined by the red line in the original image. (d) The gray level profile along the red line in (c).

CHAPTER 2

GEOLOGY OF THE ROSEMONT MINING DISTRICT

The Rosemont mining district (Figure 2.1), is located 50km southeast of Tucson , Arizona. A detailed image analysis of this area in the Santa Rita Mountains using the NS-001 data was made by Abrams and Brown (1983) to enhance surficial iron oxides and clays associated with hydrothermal alteration. The Rosemont mining district is underlain by Precambrian granodiorite, by a sequence of Paleozoic sedimentary rocks, by the Cretaceous Bisbee Group, by two intrusive plugs of Paleocene age, and by Cenozoic gravel and conglomerate. A generalized geologic map of the study area (Figure 2.2) , emphasizing both structural and lithologic features, was made based on Drewes' report (1972a).

Stratigraphy

The stratigraphy of the Rosemont mining district (Figure 2.3) includes Cenozoic gravel and conglomerate and a thick sequence of Paleozoic strata, which consists mainly of limestone, with lesser quartzite, dolomite, siltstone, arkose, and shale.

The Cenozoic gravel, called the basin-fill gravel by E.S. Davidson, M.E. Cooley, and E.F. Pashley (oral commun. with H. Drewes, 1963-68), is a part of the extensive gravel around the Santa Rita Mountains. The basin-fill gravel in the study area consists mainly of cobble, pebble, or boulder gravel of the piedmont facies. Most of the gravel was derived from the Precambrian granodiorite, whereas only a small amount of the gravel was derived from the Paleozoic sedimentary rocks that lie immediately west (Drewes, 1972b).

The Cretaceous rocks include the Glance Conglomerate and the Willow Canyon Formation containing arkose, andesite, and conglomerate. Drewes (1972a) concludes that argillic-pyritic hydrothermal alteration associated with mineralization occurs in Cretaceous Arkose near the Rosemont porphyry copper deposit.

The Paleozoic rocks in the study area include Bolsa Quartzite, Arigo Formation, Martin Formation, Escabrosa Limestone, Horquilla Limestone, Earp Formation, Colina Limestone, Epitaph Dolomite, and Scherrer Formation. In the study area, tactite alteration was studied chiefly in the Escabrosa Limestone, Horquilla Limestone, and Colina Limestone by McNew (1981). Tactite, consisting of abundant silicate alteration minerals derived from the alteration of carbonate rocks, is a favorable host for mineral

exploration. McNew (1931) reports that tactite alteration is quite extensive in the Horquilla Limestone and a large portion of the copper mineralization in the area occurs in this formation.

Igneous Rocks

Two plugs of quartz latite porphyry of Paleocene age occur in the study area. Considerable wall rock alteration and sulfide mineralization occur in the host rocks adjacent to these intrusions. Both the quartz latite porphyry and the host rocks mentioned above contain anomalous amounts of several base and noble metals which are of economic value.

Structural Geology

The structural history of the Rosemont mining district is complicated. The following description of the structural events is from Popoff(1940), Drewes(1972a), and McNew(1981).

Popoff reports that the complex structural history in the study area can be divided into several periods.

1. The pre-Cambrian folding or faulting. They have been obscured by the Laramide orogeny. However, the pre-Cambrian granodiorite intrusion in the study area may be related to this period.

2. Monoclinical structure during the Appalachian orogeny (late Paleozoic or early Mesozoic time).
3. Laramide north-south and east-west structures accompanying an intrusion of quartz-monzonite porphyry and mineralization.

Three major north-south structures form the most important structural features in the Santa Rita Mountains. They are not well exposed on the surface and are displaced by a series of east-west fault zones.

The Santa Rita fault (Thrust fault II in Drewes' report) is the major geologic structure associated with the lead-zinc and gold-silver deposits (McNew, 1981). It also forms the western limit of the outlined copper ore body in the study area.

The Deering Spring fault, which forms the border of the exposure of Paleozoic rocks and Cenozoic gravel and conglomerate in the southern half of the study area, is a north-south-trending normal fault and dips steeply to the east.

Thrust fault I forms the western limit of the exposure of the Paleozoic strata. It overlies pre-Cambrian granodiorite and underlies Paleozoic rocks. The thrust fault dips mostly eastward, and the dip value ranges from low value in the southern study area to about 90 degrees in the northern part. Secondary copper minerals can be found

in the north and west of the Rosemont mining district along the fault gulch.

The east-west faults followed north-south faulting, and separated the Paleozoic rocks into several blocks. The faults can be traced on the surface by depressions, fault breccia, and crushed rocks. Since they were later intruded by quartz-monzonite porphyry, which was followed by mineralization, many prospects are situated in these faults.

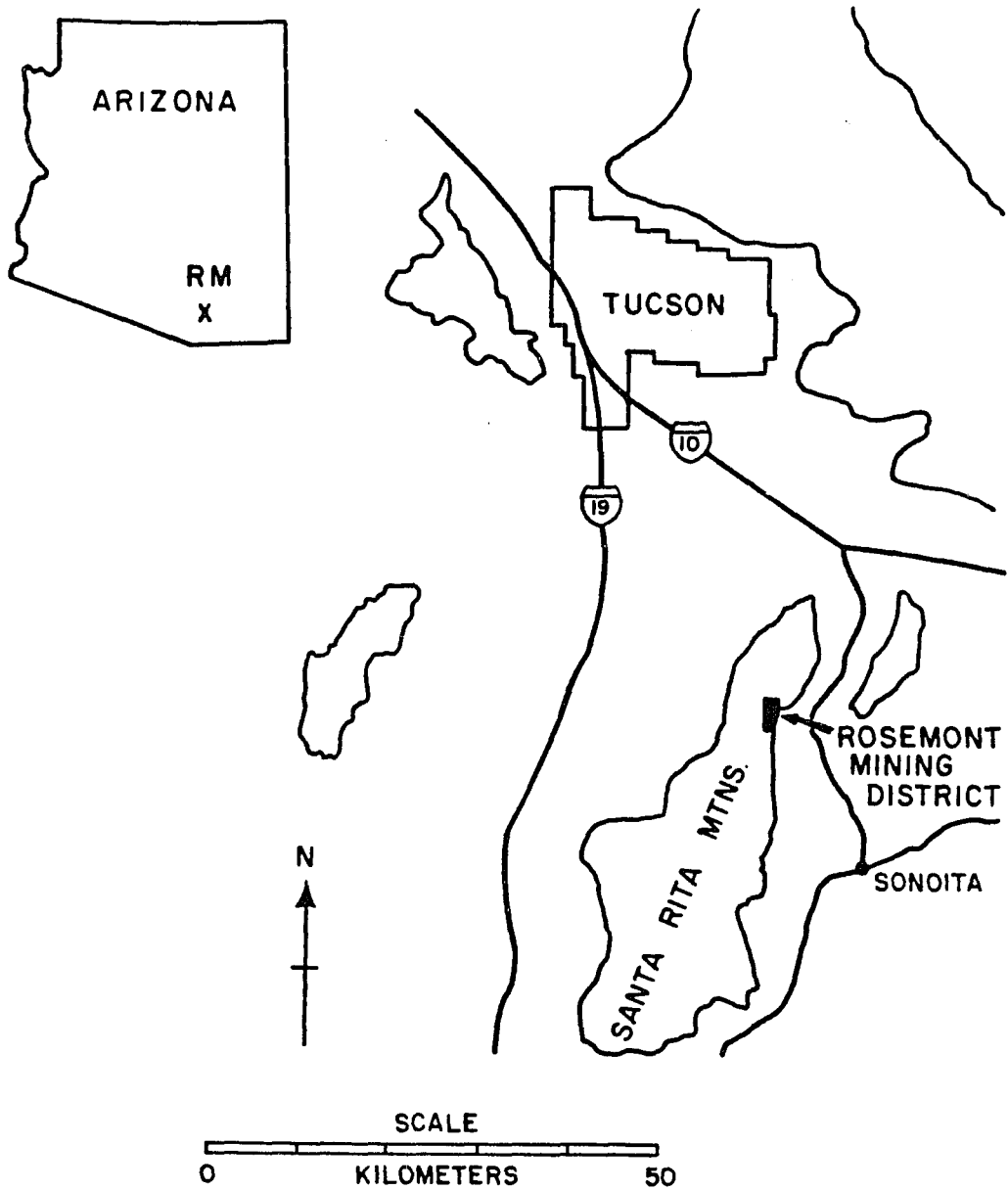


Figure 2.1. Location map of the Rosemont mining district.
(from McNew, 1981)

EXPLANATION

- C Tertiary and Quarternary
Gravel and Conglomerate
- M Tertiary Intrusives of Greaterville
- H Tertiary Intrusives of Helvetia
- A Cretaceous Willow Canyon Formation
- L Paleozoic Sedimentary Rocks
- Q Cambrian Bolsa Quartzite
- G Pre-Cambrian Granodiorite
- I Thrust Fault I
- II Santa Rita Fault
- D Deering Spring Fault
- EW East-West Fault
- K Dikes
- Contact
- Fault
- Thrust Fault



Figure 2.2. Generalized geologic map of the Rosemont mining district.
(modified from Drewes, 1972a)

Age	Formation	Thick. meters	Section	Description
Cretaceous	Willow Canyon Formation	670+		Arkosic sandstone and siltstone, andesite, volcanic- and chert-cobble conglomerate.
	Glanca Conglomerate	0-460		Limestone and granodiorite cobble conglomerate.
Permian	Rainvalley F.	0-90		Limestone, dolomite, sandstone.
	Concha Limestone	120-175		Limestone, thick-bedded, cherty.
	Scherrer Formation	220		Quartzite, fine-grained, dolomite, minor siltstone at base.
	Epitaph Formation	305		Limestone, marl, siltstone, dolomite, local gypsum and quartzite.
	Colina Ls.	105		Limestone, medium-thick-bedded.
	Earp Formation	245		Siltstone, shale, some sandstone and limestone.
Pennsylvanian	Horquilla Limestone	245		Limestone, thin-massive-bedded, siltstone, minor shale and conglomerate at base.
Miss.	Escabrosa Limestone	170		Limestone, thick-massive-bedded, local chert.
Dev.	Martin F.	120		Dolomite, limestone, siltstone, some sandstone.
Cambrian	Abrigo Formation	225-275		Siltstone, shale, limestone, and quartzite, thinly interbedded.
	Bolsa Qtz.	140		Quartzite, coarse-grained.
pc	Conf. Gr.			Granodiorite porphyry.

Figure 2.3. Stratigraphy column of the Rosemont district. (from McNew, 1981)

CHAPTER 3

ANALYSIS OF REMOTE-SENSING DATA

This chapter will describe the imagery used to test the image processing techniques.

Thematic Mapper Simulator Data

Digital images used in this project were acquired with the Visible-Near Infrared (VNIR) scanner, NS-001, at an altitude of 5,000 m in October of 1978 as part of the NASA/JPL/GEOSAT project (Abrams, Brown, Lepley, and Sadowski; 1983). The NS-001 scanner, which was designed to simulate the Landsat-4 Thematic Mapper (TM) scanner, provides digital image data having higher spatial, spectral, and signal resolution than Landsat multispectral scanners (MSS) as summarized in Table 3.1. Therefore the thematic mapper simulator data can provide more lithologic information and spatial detail than the MSS data.

Facilities and Software Available

Important facilities, image processing software, and image data required for the project are described below.

- A. The Cyber 175 at the University Computer Center.
- B. The PDP-11/70 computer (Digital Equipment Corp.) and the image display system, International Image System-Model 70 (Stanford Technology Corp.), at DIAL (Digital Image Analysis Laboratory).
- C. Image processing software packages : SADIE 2.4 (System at Arizona for Digital Image Experimentation), and System 511 (DIAL).
- D. Main programs
 1. Program MPCT, which was modified from the new version of SADIE 2.4, generates the principal component images and computer outputs including covariance matrix, correlation matrix, eigenvectors, and eigenvalues.
 2. Function subroutine TFTEX, written by Dr. R. A. Schowengerdt, calculates the co-occurrence matrices for the center pixel within a window and generates co-occurrence matrix features.
 3. Program TETRA was developed for textural transformation features.

Analysis of the TMS Data Structure in the Study Area

Four bands were chosen from the original 8-band NS-001 data as the input for the principal components analysis. Band 8, which is a thermal infrared band, was excluded during the analysis because of the mix of reflected and emitted energy characteristic of that

spectral band. Table 3.2 and Table 3.3 provide the statistical information (mean, variance, range of the gray levels, and correlation matrix) that characterizes the probability distribution of pixel gray levels in the remaining seven bands. The span, which is associated with the contrast, of band 1 is the lowest. In addition, the scattering effects of band 1, the band in the shortest wavelength portion (0.44 - 0.54 μm), is more significant. For these reasons, band 1 was also excluded from the principal components analysis. In Table 3.3 (first column ignored), the smallest values 0.711, 0.804, and 0.806 indicate that bands 2, 4, 6, and 7 are the less-correlated bands. The correlation between the two visible bands (2 and 3) and between the two near infrared bands (6 and 7) are the highest (0.965 between bands 2 and 3; 0.964 between bands 6 and 7), whereas the correlation between the visible and the near infrared bands is relatively low. Figure 3.1 demonstrates the scattergram of the two TMS visible bands having the highest correlation, and the scattergram of the visible and the near infrared bands having the lowest correlation. Bands 3, 4, 6, and 7 were chosen for the principal components analysis based on these representations.

Table 3.1. Characteristics of two remote sensing systems.

Landsat-4 MSS			NS-001 Scanner	
Spectral bands (μm)	4	0.5-0.6	1	0.45-0.52
	5	0.6-0.7	2	0.52-0.60
	6	0.7-0.8	3	0.63-0.69
	7	0.8-1.1	4	0.79-0.90
			5	1.00-1.30
			6	1.55-1.75
			7	2.08-2.36
			8	10.40-12.50
Spatial resolution (m)	80x80		10x10	
Bits/pixel	6		8	

Table 3.2 Statistical parameters of the probability density function of gray levels in the original NS-001 channels of the Rosemont mining subimage.

Band	Mean	Variance	Minimum	Maximum	Span
1	99.4	305.8	55.0	254.0	199.0
2	99.7	486.1	35.0	254.0	219.0
3	89.6	701.8	16.0	254.0	238.0
4	141.8	553.8	45.0	254.0	209.0
5	137.5	453.4	41.0	254.0	213.0
6	118.2	668.9	28.0	255.0	226.0
7	125.3	412.5	55.0	254.0	200.0

Table 3.3 Correlation Matrix of the original NS-001 channels of the Rosemont mining subimage.

BAND	1	2	3	4	5	6	7
1	1.000	0.964	0.904	0.812	0.789	0.784	0.730
2	0.964	1.000	0.965	0.888	0.871	0.859	0.806
3	0.904	0.965	1.000	0.859	0.924	0.941	0.905
4	0.812	0.888	0.859	1.000	0.893	0.804	0.711
5	0.789	0.871	0.924	0.893	1.000	0.956	0.897
6	0.784	0.859	0.941	0.804	0.956	1.000	0.964
7	0.730	0.806	0.905	0.711	0.897	0.964	1.000

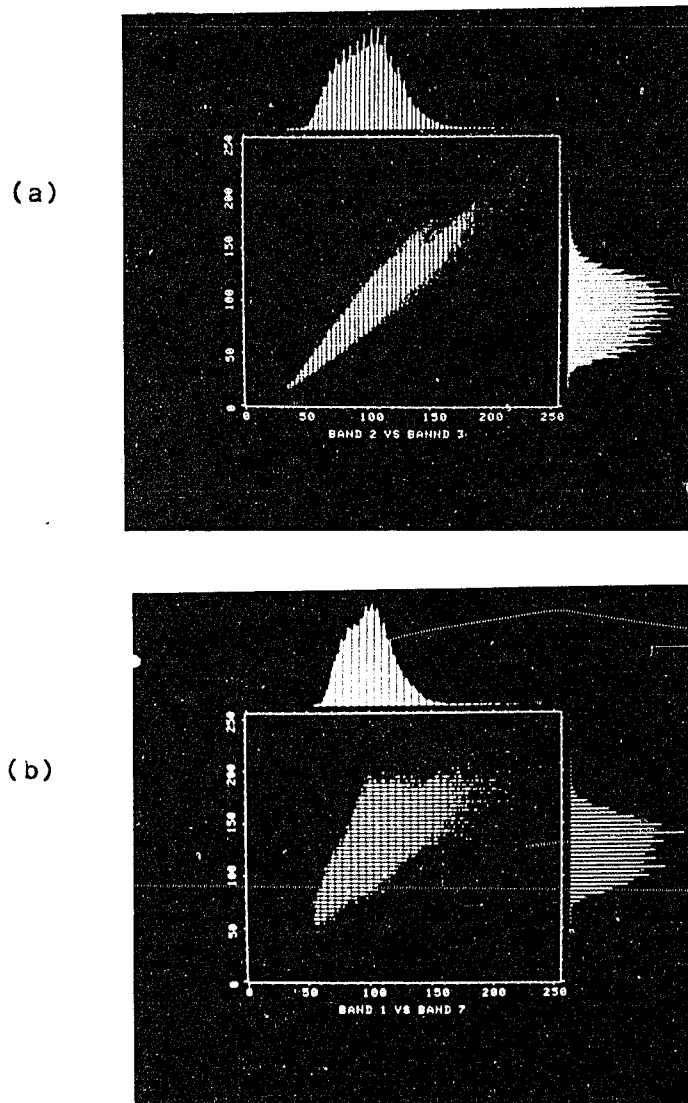


Figure 3.1. (a) Scattergram of the two TMS visible bands having the highest correlation (0.965 between bands 2 and 3). (b) Scattergram of the visible and the near infrared bands having the lowest correlation (0.730 between bands 1 and 7).

CHAPTER 4

PRINCIPAL COMPONENTS ANALYSIS

Geologic information on images usually consists of two forms, spectral and textural. The principal components analysis was chosen to enhance the spectral information. This technique enhances the tonal variations resulting from variations in the reflectance of different lithologic units (Fontanel, 1975; Jenson and Waltz, 1979; Kahle, 1980; Richard, 1984). The principal components (or Karhunen - Loeve) transformation is a data compression technique which can be applied to multispectral images to reduce spectral redundancy among individual bands (Gonzalez and Wintz, 1977; Jenson and Waltz, 1979; Schowengerdt, 1983). It is also frequently used for image enhancement, pre-classification, and noise reduction.

Geometrically, the principal components transformation is a linear orthogonal transformation to rotate and shift the coordinate axes of the original n-dimensional probability density function (PDF) to create uncorrelated principal component images with independent axes (Fig. 4.1). An analogy of the principal components analysis was given by Jenson and Waltz (1979). Suppose

one has a tube full of ping-pong balls having different colors. Observing the unprocessed images is like observing the tube from one end; only the end ball is clearly defined. Observing the principal component images is like observing the tube sidewise; all the balls are apparent. The mathematics of this statistical technique is associated with the covariance matrix of the original data and its eigenanalysis. The principal component images are ordered by decreasing gray level variance; therefore, the first principal component image has the greatest contrast and the most information content based on the assumption that the variance of a certain image feature could be regarded as a measure of information content of that image feature (Jenson and Waltz, 1979). The detailed mathematics of the principal components technique can be found in the references (Jenson and Waltz, 1979; Siegal, 1980). In this thesis only the numerical characteristics of the principal components are included in the following sections.

A subimage in the Rosemont mining district of 512 by 512 pixel size was subsampled from the original TMS data (bands 3, 4, 6, and 7). The numerical characteristics of the principal components technique obtained from the computer output includes the covariance matrix (K_{ij}), the correlation matrix (C_{ij}), the eigenvalues of K_{ij} , and the eigenvectors.

Covariance, in this case, could be used as a measure of the scatter between two bands (Jenson, 1979). Since the principal components analysis is a transformation of the original covariance matrix to a diagonal covariance matrix (i.e. for all $i \neq j$, $K'_{ij} = 0$), the original covariance matrix has to be determined first. The covariance matrix of the Rosemont mining district subimages is

$$K = \begin{matrix} 701.8 & 507.7 & 526.9 & 646.0 \\ 507.7 & 553.8 & 417.8 & 435.7 \\ 527.0 & 417.8 & 453.4 & 521.0 \\ 646.0 & 435.7 & 521.0 & 668.9 \end{matrix}$$

The diagonal elements 701.8, 553.8, 453.4, and 668.9 in the covariance matrix represent the variance of individual bands; the other elements represent the covariance between bands. In this case, the total variance (or total information content), the sum of the diagonal elements, is about equally distributed over the original four-band data.

The correlation matrix, defined by

$$C_{ij} = K_{ij} / (K_{ii} K_{jj})^{1/2}, \quad i, j = 3, 4, 6, 7$$

is then

$$C_{ij} = \begin{matrix} 1.000 & 0.814 & 0.934 & 0.943 \\ 0.814 & 1.000 & 0.834 & 0.716 \\ 0.934 & 0.834 & 1.000 & 0.946 \\ 0.943 & 0.716 & 0.946 & 1.000 \end{matrix}$$

Theoretically the correlation between bands determined by the correlation matrix C_{ij} can range from -1 to +1 (Fig. 4.2). A positive C_{ij} occurs when bands i and j are positively correlated; a negative C_{ij} occurs when bands i and j are negatively correlated; if bands i and j are completely independent of each other, there is no correlation between them and $C_{ij} = 0$. When bands i and j are highly correlated, the gray level distribution for one band can be used to predict the corresponding gray level distribution for the other band. From the correlation matrix of the Rosemont subimages, bands 3, 4, 6, and 7 are highly and positively correlated; they are numerically and visually similar. Therefore it is difficult to detect the tonal variations resulting from variations in the reflectance of different lithologic units among original multispectral imagery.

The eigenvalues of K , which correspond to the lengths of the eigenvectors (Figure 4.3), are 2143.6, 180.3, 3.94, and 1.47. These eigenvalues, arranged by decreasing order, represent the variance (i.e. width of the gray level distribution in each one dimensional PDF) of individual transformed images. The percentage of information content (or total variance) (Fontanel, 1975; Santisteban, 1977) derived from the eigenvalues for the four components is listed below:

First component: 92.0 %

Second component: 7.7 %

Third component: 0.2 %

Fourth component: 0.1 %

It can be seen that the first two components account for about 99.7% of the total variance in the original image data. As a result, the goal to compress image information into fewer dimensions by the principal components analysis can be accomplished by rearranging the total variance in the original data.

The weights for eigenvectors, which lie on the transformed axes (Figure 4.3), are shown in Table 4.1. The longest eigenvector is chosen to be the first principal component; the second longest eigenvector is chosen to be the second principal component. It can be observed that the first principal component image is taken nearly equally from the original 4-band data. Hence, the first transformed image is simply a weighted average image. The second principal component image is dominated by the band 4 data. It shows the contrast (variations) of the original band 4 with bands 6 and 7. Similarly, the contrast between the original bands 3 and 6 is shown in the third component image. The digital image processing results that show the relationships mentioned above will be presented and discussed in detail in Chapter 6.

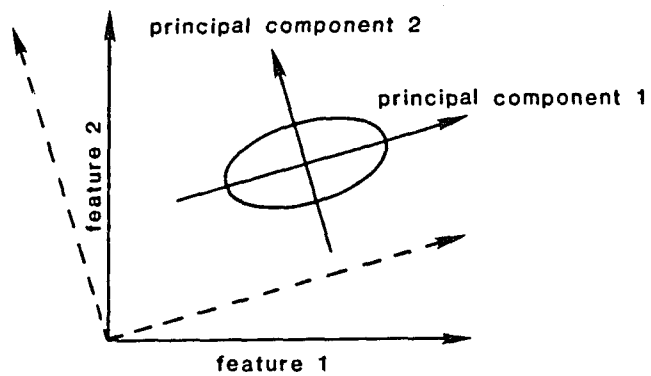


Figure 4.1. Rotation and shift of the coordinate axes in two dimensions.
(from Schowengerdt, 1983)

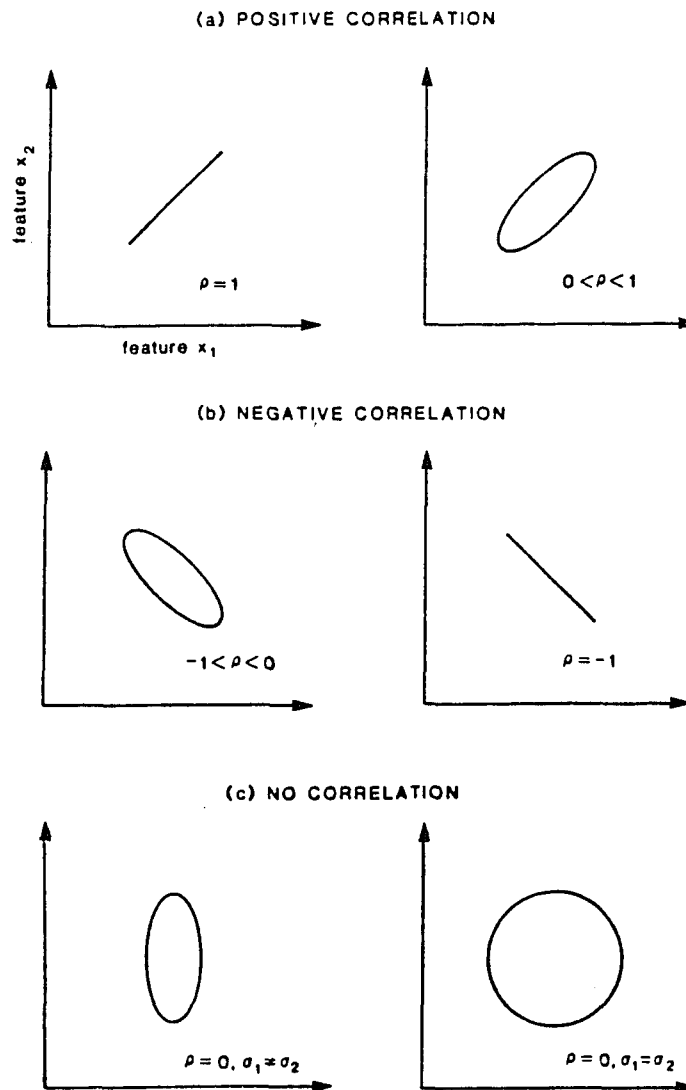


Figure 4.2. Two dimensional correlation diagrams.
(from Schowengerdt, 1983)

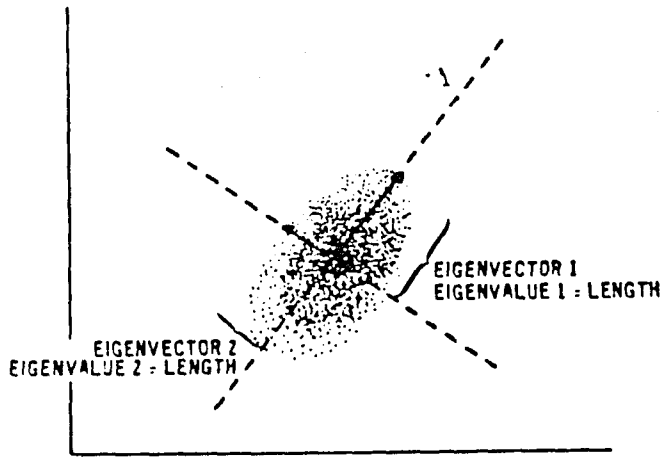


Figure 4.3. Eigenvectors and eigenvalues in two dimensions.
(from Jenson, 1979)

Table 4.1 Weights for Eigenvectors

TMS BANDS	PC1	PC2	PC3	PC4
3	0.573	-0.032	-0.711	-0.406
4	0.431	0.857	0.190	0.209
6	0.549	-0.334	0.670	-0.371
7	0.428	-0.390	-0.099	0.809

CHAPTER 5

TEXTURE ANALYSIS

Image processing techniques that accomplish semi-automated or automated linear-features mapping are needed in order to reduce the problem of variability and subjectivity in lineament interpretation (Podwysocki et al., 1975). Gradient operators enhance edges and boundaries associated with landforms. The co-occurrence matrix (COM) and textural transformation, two statistical approaches which use a moving window computer algorithm, are used herein to automatically map linear features associated with geologic structure and to characterize "edge density" which aids the lithologic interpretation in this study. "Edge density" represents the density of landform lineaments which may reflect differences in surficial materials.

Gradient Operator

The gradient, an approximation to the first partial derivative (Ballard and Brown, 1982), is the most common edge operator. Gradient images were created by convolution of the first principal component image using filter weights shown in Figure 5.1(a) and (b). The gradient magnitude at

each pixel in the first principal component image was calculated by determining the gray level difference of the two pixels on either side of a pixel in two orthogonal directions (vertical and horizontal).

Kernel $\Delta 1$ enhances linear features in the vertical direction, whereas kernel $\Delta 2$ enhances linear features in the horizontal direction. The gradient magnitude image M which enhances all directional linears were created by

$$M(x,y) = (\Delta 1^2 + \Delta 2^2)^{1/2}$$

where

$$\Delta 1 = f(x-1,y) - f(x+1,y)$$

$$\Delta 2 = f(x,y-1) - f(x,y+1)$$

$f(x,y)$ is the gray level of pixel (x,y) .

Co-occurrence Matrix

The application of co-occurrence (spatial gray level dependence) to digital images has been studied by some investigators. Julesz (1962) first used co-occurrence statistics to discriminate textures. Rosenfeld and Troy (1970) utilized a co-occurrence matrix for each fixed distance and angular spatial relationships. Haralick et al. (1973) used co-occurrence matrices to characterize texture in satellite, aerial, and microscopic images. Jensen (1979) applied co-occurrence matrices to classify land cover at the urban fringe. Schowengerdt

(1981) utilized co-occurrence matrices as an example of the statistical approach to texture description.

Co-occurrence texture features are derived from the co-occurrence matrices which describe texture using spatial distribution and spatial dependence (refer to Fig. 5.3c) among the gray levels in a local region (Haralick, 1979).

For any digital image $f(x,y)$, each pixel is characterized by a sample pixel coordinate x and a sample line coordinate y . If vector $d = (dx,dy)$ is considered as a vector measured from a center pixel within a square window to each adjacent pixel in the (x,y) plane, it is possible to compute the joint probability density of the pair of gray levels that occur at pairs of pixels separated by d within a window. Figure 5.2 depicts four independent angles (separation vectors) for D (distance between pixels within a window) equal to one. The joint probability density may be characterized by an array $A(i,j)$, which depicts the probability that the pairs of gray levels (i,j) have at separation d . Since the original image was quantized to 16 gray levels(0-15), the dimension of the array $A(i,j)$, the co-occurrence matrix, is 16 by 16. In order to calculate the array A for a local area (i.e. a window), the number of times each pair of gray levels occurs at separation $d(x,y)$ in the window has to be counted (Jensen, 1979). For example, Figure 5.3 depicts a simple

case to calculate the co-occurrence matrices. Figure 5.3(a) depicts a 4 by 4 image that has been quantized to only 4 gray levels; Figure 5.3(b) defines the location in the co-occurrence matrix; Figure 5.3(c) describes the calculation of the co-occurrence matrices at four different angles (Haralick, 1979). During the process of calculation, four co-occurrence matrices for four different angles (-45° , 0° , 45° , 90°) at $D = 1$ may be averaged to minimize the dependence of calculated texture features on angle (Schowengerdt, 1981).

From the above explanation, it is easy to understand that the co-occurrence matrix may be regarded as a kind of gray level transition probability matrix. There are four parameters defining the co-occurrence matrix (Schowengerdt, 1981).

1. The number of gray levels in the image, which characterizes the dimension of the co-occurrence matrix,
2. The distance between pixels used to generate the co-occurrence matrix,
3. The angle (separation vector) between pixels used to generate the co-occurrence matrix, and
4. Spatial window size used in the computer algorithm.

The co-occurrence matrix features were derived from the first principal component image, because it has the

largest gray level variance (the most information content) obtained from the original multispectral imagey, and the least noise. Before the co-occurrence matrices were computed, the first principal component image was quantized to 16 gray levels.

Two texture features were derived from the co-occurrence matrices:

1. Angular second moment (ASM)

$$ASM = \sum_i \sum_j (p(i,j))^2$$

2. Contrast (CON)

$$CON = \sum_i \sum_j (i-j)^2 P(i,j)$$

where

(i,j) indicates a certain location in the co-occurrence matrix. P(i,j), the element of the co-occurrence matrix, represents the probability of transition from gray level i to gray level j (Schowengerdt, 1981).

The major software in this experiment, FUNCTION TFTEX, was written by Dr. Schowengerdt to calculate co-occurrence matrices and two texture features (ASM, and CON) and was programmed for a pixel-by-pixel neighborhood calculation.

A moving window algorithm (subroutine TEXT) was utilized to implement the neighborhood calculations (Figure 5.4). During computation, four co-occurrence matrices (0^o,

45° , 90° , -45° were calculated for each center pixel within the window. The co-occurrence matrices for four angles were averaged to enhance all directional linears (Schowengerdt, 1981). After the co-occurrence matrices were computed, a specified feature value, say CON, was calculated based on the equation

$$CON = \sum_{ij} \sum (i-j)^2 P(i,j)$$

for the center pixel. The same calculation was then repeated for the rest pixels of the unprocessed data. Although programmed using efficient recursive rules, the co-occurrence calculation is time consuming. The computation time needed for different image sizes to obtain different texture features is depicted in Table 5.1. In general, it takes about 2 hours on the PDP 11/70 to create a co-occurrence matrix feature when the image size is 512 by 512. Furthermore, the parameters chosen to define COM in this experiment are depicted in Figure 5.5.

Textural Transformation

The textural transformation is a statistical approach to extract textural information. Hsu (1978) applied the textural transformation and a Mahalanobis distance algorithm to classify digitized aerial photographs from a single spectral data band. His transformation is useful (85-90% accuracy) for thematic mapping. Irons and

Petersen's textural transformation features (1981) were based on Hsu's work (1978). They applied their textural transformation and a minimum distance classifier to classify a Landsat image. Several of their textural transformation features proved to be valuable as edge detectors for image enhancement; however, the features were not very useful for thematic mapping.

In order to construct textural transformation features, a moving window algorithm is used. Each pixel of the first principal component image is regarded as a center pixel within a window (3 by 3 pixels in size in this experiment). Four steps were performed to generate a textural transformation feature. First, the gray levels of pixels within a window were extracted from the first principal component image. Second, choose one texture feature at a time from the following features:

1. Standard deviation (STD)

$$STD = ((\sum_{ij} (X_{ij} - \mu)^2) / (n - 1))^{1/2}$$

2. Range (RAN)

$$RAN = \max(X_{ij}) - \min(X_{ij})$$

3. Mean of squared length differences (MSQ)

$$MSQ = (\sum_{ij} (X_{ij} - X_c)^2) / (n - 1), \text{ where}$$

X_{ij} indicates the gray level for pixel (i,j) in the first principal component image; n is equal to the number of pixels within a window; μ represents the mean gray level

within a window; X_c is the gray level of the center pixel; The values, $\max(X_{ij})$ and $\min(X_{ij})$, are the maximum and the minimum gray level within a window.

Third, assign the value calculated (STD, RAN, or MSQ) to the center pixel as a local property value. Finally, repeat the same procedure to calculate the local property values for the other center pixels.

This algorithm, compared to the co-occurrence matrix algorithm, is less complicated. It takes 30 minutes to generate a textural transformation feature when the image is 512 by 512 pixels in size, whereas it takes about two hours to create a co-occurrence matrix feature.

(a) $\Delta 1 =$

0	0	0
1	0	-1
0	0	0

(b) $\Delta 2 =$

0	1	0
0	0	0
0	-1	0

Figure 5.1. Convolution kernels used to construct (a) A first derivative image enhancing the vertical direction linear features, and (b) A first derivative image enhancing the horizontal direction linear features.

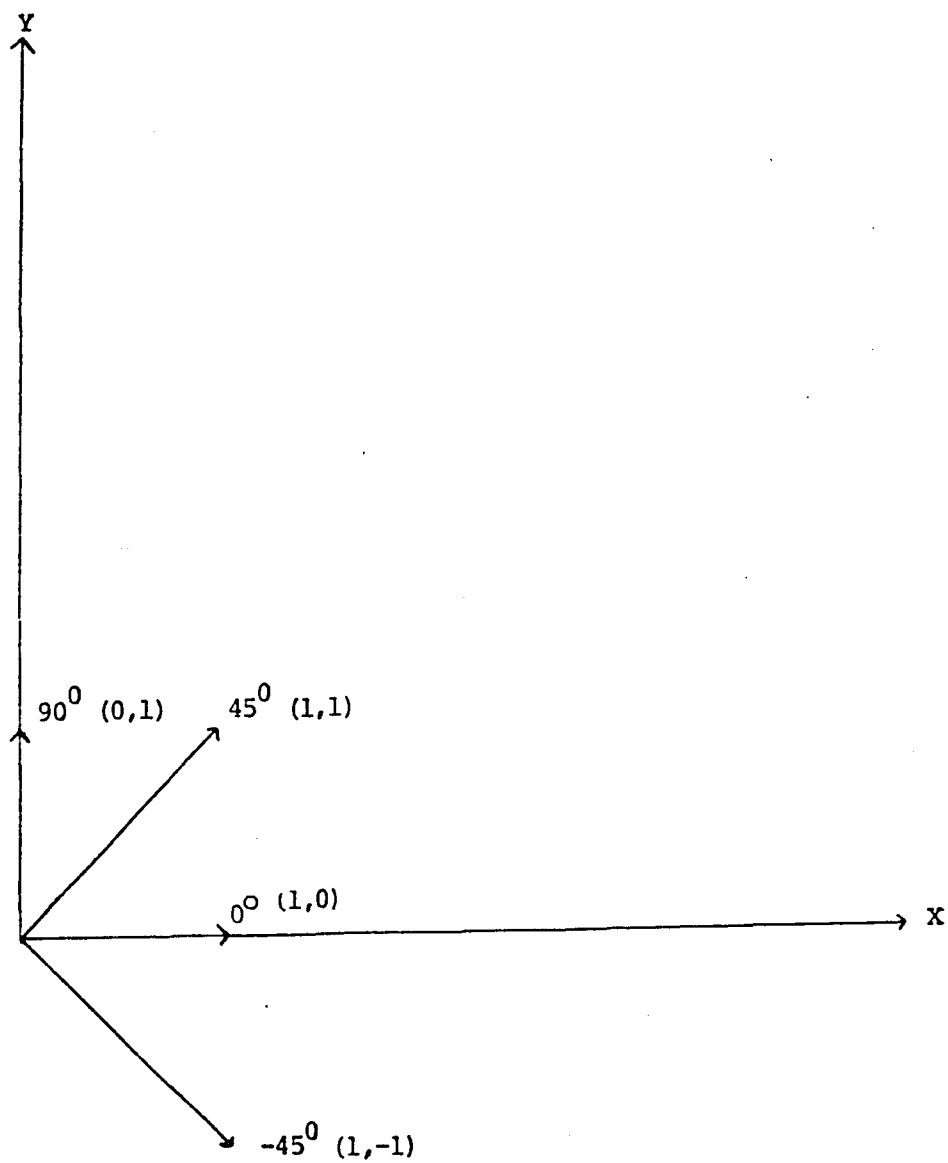


Figure 5.2. Four independent angles (separation vectors) for $D = 1$.

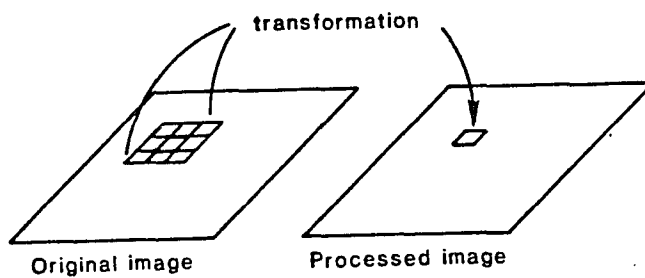
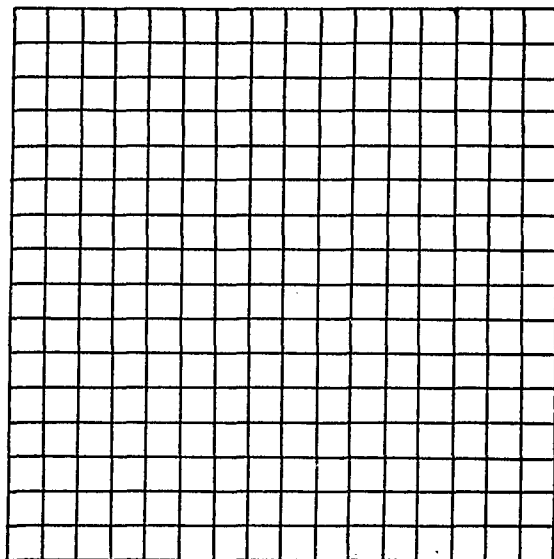
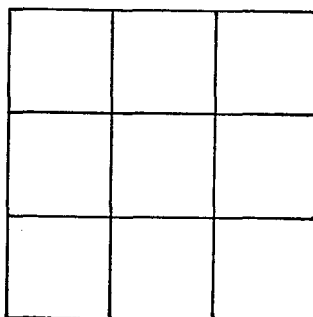


Figure 5.4. Moving window algorithm. Gray levels of pixels within a window are used to measure a specified texture feature.
(from Schowengerdt, 1983)



5.5a. Dimension of COM.



5.5b. Spatial window size (3 by 3)

Figure 5.5. Parameters defining the COM in this experiment
(from Schowengerdt, 1981).

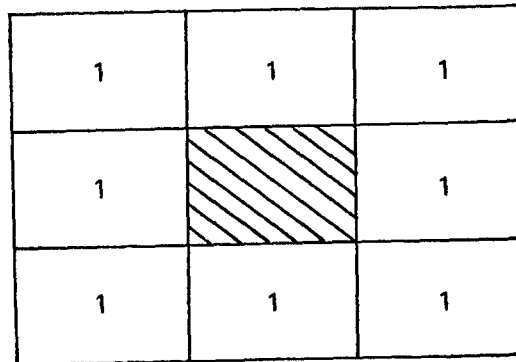
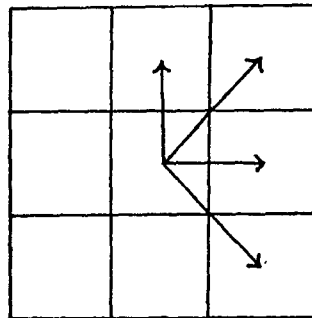
5.5c. Distance ($D = 1$)5.5d. Angle ($A = 0^\circ, 45^\circ, 90^\circ, -45^\circ$).Figure 5.5. Parameters defining the COM in this experiment.
(from Schowengardt, 1981)

Table 5.1. Computation time for the co-occurrence matrix features with different image sizes.

* *** **	ASM	CON
16X16	13"	14"
32X32	35"	36"
64X64	1'40"	1'42"
128X128	6'55"	8'30"
256X256	24'30"	30'00"

* - Texture feature

** - Image size

*** - Computation time

CHAPTER 6

RESULTS AND DISCUSSION

This chapter presents digital image processing results generated from TMS data in the study area. The results may be divided into two parts: principal component images and texture features.

Principal Component Images

One of the objectives in this project is to investigate the capability of the principal components analysis to contribute to lithologic separations. The principal component images were produced by using TMS data for a 2.5 by 5.5 km area in the Rosemont mining district. The hydrothermal altered regions in the study area contain the Paleozoic sedimentary rocks and the Cretaceous rocks. The Paleozoic rocks are a favorable host for mineralization. Argillic-pyritic hydrothermal alteration associated with mineralization occurs in Cretaceous Arkose. Four bands (bands 3, 4, 6, and 7) were chosen from the original 8-band data to form the input data; therefore, four output principal component images (PC1, PC2, PC3, and PC4) can be created from the input data. The utilization of TMS bands 6 and 7 (1.55-1.75 μ m and 2.08-2.36 μ m).

respectively) in the principal components analysis makes it possible to locate the areas of interest. The 1.65 μ m band (band 6) is useful in geologic applications because altered rocks have their highest reflectance within this spectral region; the 2.2 μ m band (band 7) is also useful because hydrous minerals have a strong absorption feature within the band (Abrams, 1983).

Several rules of thumb are used in order to interpretate the principal component images.

1. The variance of a certain image feature can be regarded as a measure of information content of that image feature.
2. The eigenvalues represent the variance in each component of the transformed images.
3. The eigenvector represents the weights of the linear transformation for each transformed image.
4. Generally, the first principal component image is simply a weighted average image, whereas the other components can be treated as images showing areas of spectral differences among original bands.
5. In addition to the variance of individual probability density functions, the principal components technique has the ability to rank the signal to noise ratio. Random noise and periodic noise that is uncorrelated between bands will be more apparent in the lower order component images (Siegal et al., 1980).

Figure 6.1 shows unenhanced original TMS images (Bands 3, 4, 6, and 7) taken in the Rosemont mining district. The area studied is shown on the left part of these images.

TMS principal component images are represented in Figure 6.2. PC1 (the first principal component image) shown in Figure 6.2(a) is highly correlated to the original data. It consists of most of the information content and is a weighted average of the original data. It contains a minimum amount of noise and appears free from striping. PC2 and PC3 (the 2nd and 3rd component images) contain a small amount of total variance, but they do show the superiority of the principal components analysis in discriminating lithologic variations; they show the separations of major rock units that are difficult to be observed from the original data.

PC2 (Figure 6.2(b)), which is dominant by band 4, shows the contrast (tonal variations) of the original bands 4 with 6 and 7. The zone of pre-Cambrian granodiorite (marked G), Tertiary intrusives of Helvetia (marked H), and Tertiary intrusives of Greaterville (marked M) showing higher reflectance in band 4 than in bands 6 and 7 is clearly brought out by the brightest tone areas. A belt of Bolsa Quartzite (marked Q) can be distinguished from the Paleozoic rocks (marked L) by its darker tone. In

addition, PC2 turns out to be like a high-pass filter; some lineaments having geologic significance and drainage patterns in the desert plain appear quite clear.

PC3 (Figure 6.2(c)) ,which is dominant by bands 3 and 6, shows the contrast between the original bands 3 and 6. The hematitic rocks associated with pyritic alteration of Cretaceous arkose showing darker tone in band 3 than in band 6 is marked by whitish - grayish tones in PC3 (marked A). The Paleozoic rocks containing mainly limestone do not show distinct tonal density variations to be marked separately and hence all of them have been grouped together under the term "Paleozoic rocks" (marked L). They show grayish tone in PC3. The Helvetia intrusives (marked H) is identified by its bright tone on the left upper corner of PC3.

Striping is the most dominant noise in the transformed images. It is especially apparent in the 4th transformed image (PC4; Figure 6.2(d)).

The principal component images provide significant information on areas having different spectral information among the original multispectral imagery. The improvements in lithologic separation are more apparent on color-composites created from the principal component images than they are on the single band format image. The result (PC321) that allows the best visual discrimination of the

lithologic units was obtained by coding the first component in blue, the second component in green, and the third component in red (Figure 6.3(a)). Another color composite (PC432; shown in Figure 6.3(b)) created by coding the second component in blue, the third component in green, and the fourth component in red can be used as an adjunct to the best color-composite mentioned above. In addition, Figure 6.3(c) represents the color composite created from the original bands 4 , 6, and 7 as a comparison to the processed color-composites. The reason why the color composites created from the principal component images may separate major rock units in the study area, apparently, is that several individual principal component images provide lithologic separations from the unprocessed data.

A geometric correction was not applied to the imagery because it is not the intent of this paper to describe the geological interpretation of the image in detail. The study is to verify the usefulness of the principal component transformation technique in lithologic separations and to apply different texture extraction algorithms to the images to see if they can enhance or automatically delineate textures. However it should be kept in mind during image interpretations that an area represented as pixels along the edge of the data is larger than the area of pixels at nadir. The identification

of rock units in the images was based on the generalized geologic map (Figure 2.2) and on the correlation between control points in the aerophotos and control points in the images. Evaluation of the principal components color composites was conducted by comparing the distribution of colors in images with the rock units in the generalized geologic map and by field checking critical areas.

Important observations made during the study of the principal component images are discussed below:

(1). Rock unit G in the principal component color-composites corresponds to pre-Cambrian granodiorite which forms the axis of the Santa Rita Mountains . It is clearly brought out by the yellowish-greenish zone on the left part of PC321. It appears dark blue in PC432. The boundary (thrust fault I) between unit G and L is characterized by the lineament that shows strong color contrast on both sides of it.

(2). Rock unit L corresponds to Paleozoic sedimentary rocks containing mainly limestone. The altered limestone beds were the most favorable rocks for copper mineralization. It is identified by its bluish-purple colors in the central part of PC321 and by its brownish-yellow colors in PC432.

(3) The Cretaceous rocks (marked A) are

characterized by vivid purple color in PC321, and by bright yellow color in PC432.

(4) The Helvetia intrusives (marked H) appears bright yellow in PC321 and white-yellow in PC432.

(5) The small yellow areas (marked M) in PC321 represent argillically altered quartz monzonite porphyry (Greaterville intrusives) associated with sulphide mineralization.

(6) Many small yellow-white areas correspond to mine dumps and cleared ground (marked R) around mines in the central part of PC321. These areas are more clearly defined in PC1.

(7) Field examinations suggest that the blue areas on the right side of PC321 correspond to Cenozoic alluvial materials (marked C).

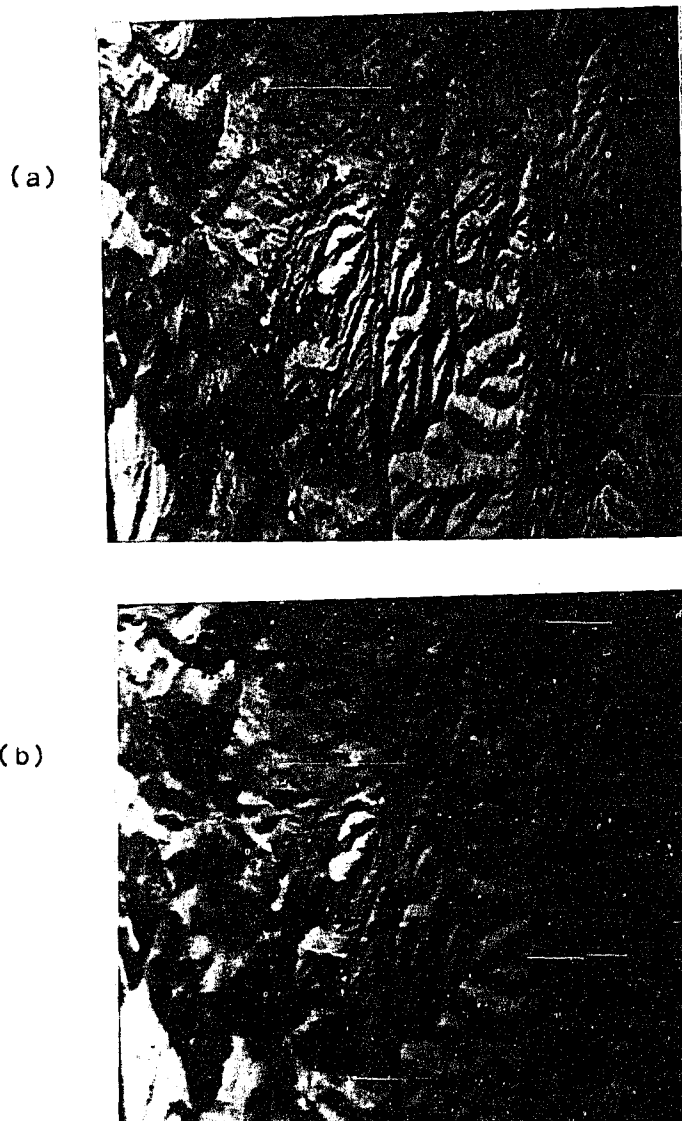


Figure 6.1. Unenhanced original TMS images of the study area. (a) Band 3 (0.63-0.69um) (b) Band 4 (0.79-0.90um).

(c)



(d)



Figure 6.1. Unenhanced original TMS images of the study area. (c) Band 6 (1.55-1.75 μ m) (d) Band 7 (2.08-2.36 μ m).

(a)

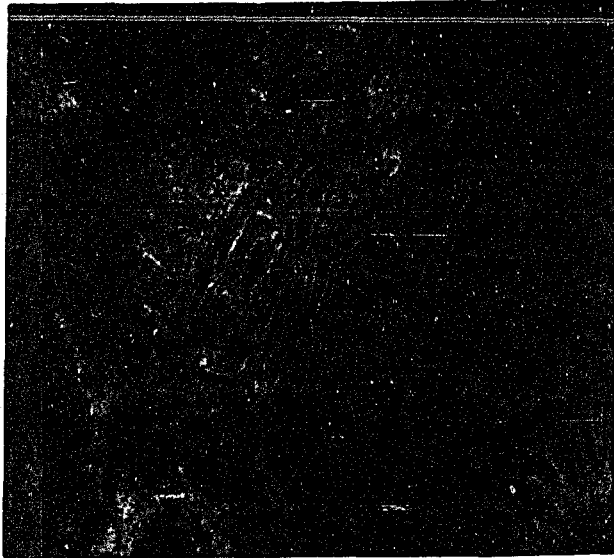


(b)



Figure 6.2. TMS (4-band data) principal component images of the Rosemont mining district, Arizona. (a) PC1, a weighted average image. (b) PC2. G = granodiorite; M = Greaterville intrusives; H = Helvetia intrusives; Q = Bolsa Quartzite; L = sedimentary rocks mainly limestone.

(c)



(d)



Figure 6.2. TMS (4-band data) principal component images of the Rosemont mining district, Arizona. (c) PC3. A = Altered Cretaceous rocks; L = Paleozoic sedimentary rocks mainly limestone; H = Helvetia intrusives. (d) PC4, having the most noise.

(a)

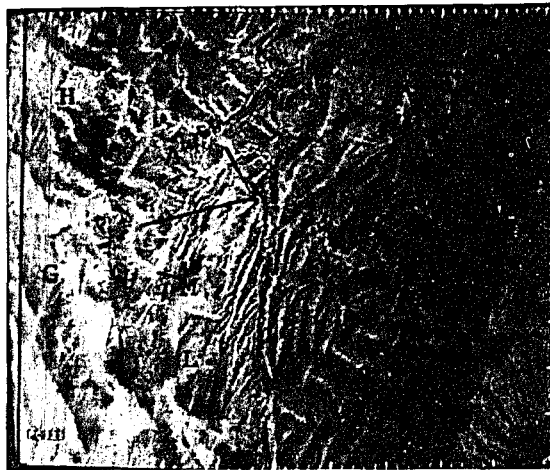


Figure 6.3a. Color composite of the first three principal components (PC1 in blue, PC2 in green, and PC3 in red). G = pre-Cambrian granodiorite; H = Helvetia intrusives; M = Greaterville intrusives; Q = Bolsa Quartzite; L = Paleozoic sedimentary rocks; A = Cretaceous rocks; C = Cenozoic gravel and conglomerate; R = Mine dumps and cleared grounds.

(b)

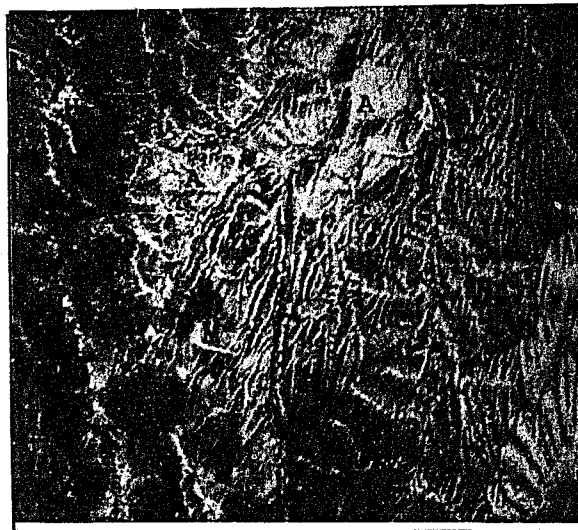


Figure 6.3b. Color composite of PC2, PC3, and PC4. (PC2 in blue, PC3 in green, and PC4 in red). G = granodiorite; H = Helvetia intrusives; M = Greaterville intrusives; Q = Bolsa Quartzite; L = sedimentary rocks mainly limestone; A = Cretaceous rocks; C = Cenozoic alluvial materials.

(c)



Figure 6.3c. Color composite of the original TMS bands.
(band 4 in red, band 6 in green, band 7 in blue).

Texture Features

Two types of texture images were generated in this project. One is gradient images; another is texture features derived from statistical approaches (co-occurrence matrix and textural transformation).

Gradient Images

Gradient operators are directional high pass filters used for semi-automated mapping of linear features. Although the gradient operator used in this project does not allow for rapid inspection of enhanced linear features in the desired direction, it does provide excellent enhanced images and variety of filter possibilities (different versions of gradient operators are discussed in Ballard and Brown, 1982).

Figure 6.4(a)-(c) show the processed results. Figure 6.4(a) and (b) depict gradient images enhancing linear features in the vertical and horizontal direction respectively. Figure 6.4(c) depicts the gradient magnitude image enhancing all directional linear features. The results produce more linear features than can be observed by interpreters from the original data. This implies that some artifacts may have been introduced in the image processing procedure; the artifacts are especially apparent in Figure 6.4(b). However, the comparison between the gradient images and the large-scale photographs of the

study area shows that in most cases, linear features can be correlated between the two.

To accomplish a successful lineament mapping based on the processed results, information collected from published geologic maps, aerophotographs, topographic maps, and field checking is needed. Figure 6.4(c) represents an interpretation overlay of the gradient magnitude image. Textural information that corresponds to local geologic structural trends in TMS data can be easily enhanced. For example, a conspicuous fault (I), represented by linear topographic ridges, was clearly defined the bright tone lineament. The Deering Spring fault (D), the Santa Rita fault (II), east-west faults (EW), and dykes (M and Y) are indicated by a relative change in tone. In addition, the two major geologic structural trends in the N-S and E-W directions can be easily observed. Extensive dissection of the desert plains (marked C) has resulted in a fine texture of erosional topography and fine-textured drainage. The parallel-angular drainage patterns are typical of the alluvial areas.

Co-occurrence Matrix Features

Figures 6.5(a) and (b) depict co-occurrence matrix features (ASM, and CON) derived from the first principal component image.

$$\text{Angular Second Moment (ASM} = \sum_{ij} P(i,j)^2)$$

By the definition of the equation, ASM (Figure 6.5(a)) may be used to describe the homogeneity of the image. In a homogeneous region such as the belt of Bolsa Quartzite (marked Q), the changes of gray levels are subtle; therefore, there are only fewer elements having large values in the co-occurrence matrices. In this region, the ASM value derived from the sum of squares of the elements in the co-occurrence matrices is larger (i.e. brighter). However, in the area having high texture content such as the alluvial region (marked C), the changes of gray levels are abrupt; therefore, there are more elements having small values in the co-occurrence matrices. The ASM texture feature value, in this case, is smaller (i.e. darker). Consequently, the bright pixels in Figure 6.5(a) represent homogeneous regions, whereas the dark pixels represent regions having tonal variations.

$$\text{Contrast (CON} = \sum_{ij} (i-j)^2 P(i,j))$$

From the equation and Figure 6.5(b), the utility of CON as an edge detector becomes apparent. The term $(i-j)^2$ in the equation makes the values of edge pixels much higher than the values of the adjacent homogeneous pixels. However, in the nonhomogeneous area, the term $(i-j)^2$ makes the area very dark in the CON image. Therefore, all the edges

and boundaries associated with landforms are enhanced by this texture feature.

Textural Transformation Features

Three textural transformation features of the local properties (STD, MSQ, and RAN) were created by using three-by-three pixel windows. Again the first principal component image was used for the computations. A negative linear intensity transformation of the texture measurements was used to obtain better visualization from the texture features.

Figures 6.6(a)-(c) present images corresponding to the standard deviation(STD), mean of squared length differences(MSQ), and range (RAN) measurements. The results show that the three texture features are almost identical; it implies that they are highly correlated.

From the displayed images, textural transformation features turn out to be useful as edge detectors for image enhancement. The edge detection capability of these texture features can be realized by considering their computational formulas. The pixel values of the texture features are zero (representing dark pixels) when there is no gray-level changes in the pixel windows; the window areas are homogeneous. The pixel values increase when gray-level changes occur in the pixel windows. They become the largest (brightest) on the boundaries between two

regions with distinct tonal variations. Since the texture features were negatively transformed, the relationships discussed above are opposite. Edges and boundaries were defined by dark segments or lines. A Range image (RAN) with a 5-by-5 window is depicted in Figure 6.6(d). It can be seen that the textural transformation features with a larger window size produce thicker linear features. A pseudocolored version of the Range (RAN) image is depicted in Figure 6.6(e). It shows the superiority of the texture features (derived from the co-occurrence matrix or textural transformation) in automated linear-features mapping.

The texture features derived from the co-occurrence matrix and textural transformation are almost identical, although the ASM image shows more spatial detail than the other features. They are highly correlated either positively or negatively. The textural transformation algorithm is more practical from a computational point of view. These two algorithms provide clearer view of textural information than gradient type images.

The co-occurrence matrix and textural transformation features are useful in several geologic applications. They provide a valuable tool for automated linear features mapping. The linear features associated with geologic structures and drainage patterns are a sample of the local structural data for a region. For example, in

Figure 6.6(c) the thrust fault I (marked I), dykes (marked Y and M), high drainage density alluvial areas (marked C), and low drainage density Bolsa Quartzite area are clearly shown.

Information on "edge density" was also provided by these texture features. "Edge density" represents the density of landform linears which may reflect rock permeability and resistance. It aids lithologic interpretation in this study. For example, in Figure 6.6(c) the pre-Cambrian granodiorite area (marked G) shows relatively medium to low edge density; A belt of Bolsa Quartzite (marked Q), the most resistant rock unit in the study area, shows low edge density; the alluvial areas (marked C) show high edge density.

The texture features derived from the co-occurrence matrix and textural transformation provide additional information that can be gained by the qualitative analysis of the length, orientation, and spatial distribution of the abundant short linear features presented in texture features. They also provide a base image for a quantitative analysis of the linears; however, more advanced image processing techniques have to be developed for a quantitative analysis.

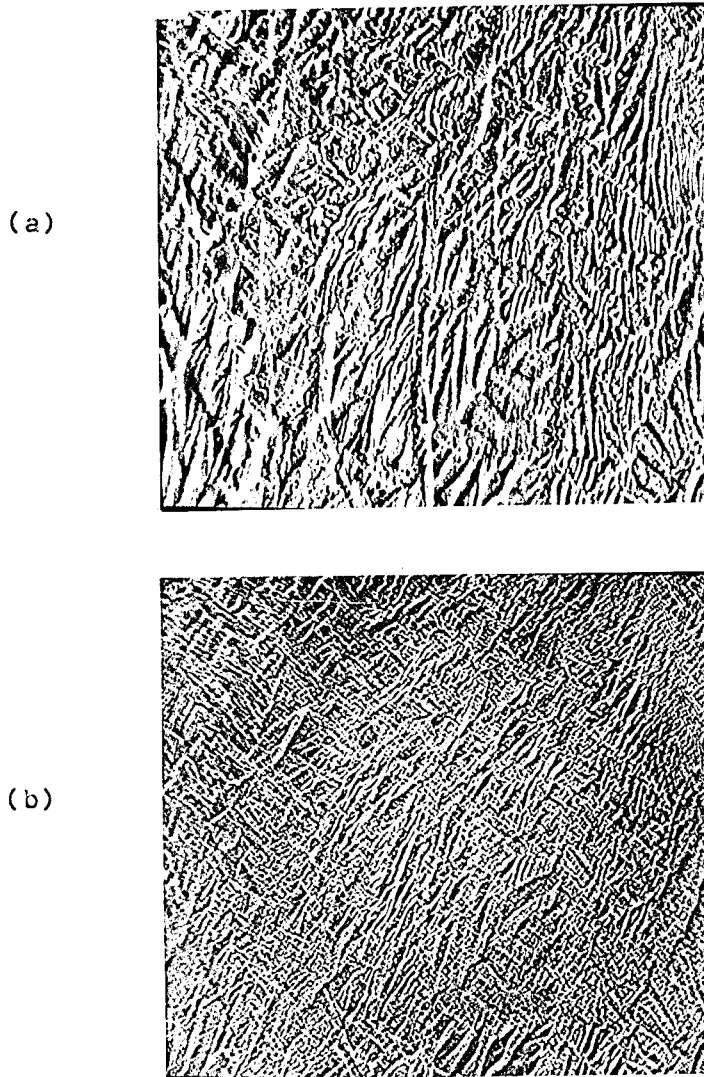


Figure 6.4. Gradient images derived from the first principal component image. (a) Gradient image enhancing linear features in the vertical direction. (b) Gradient image enhancing linear features in the horizontal direction.

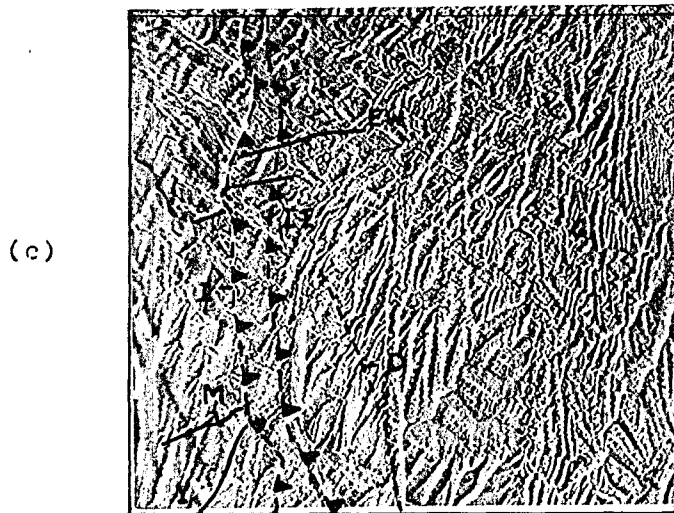


Figure 6.4. Gradient images derived from the first principal component image. (c) Gradient magnitude image enhancing all directional linear features.

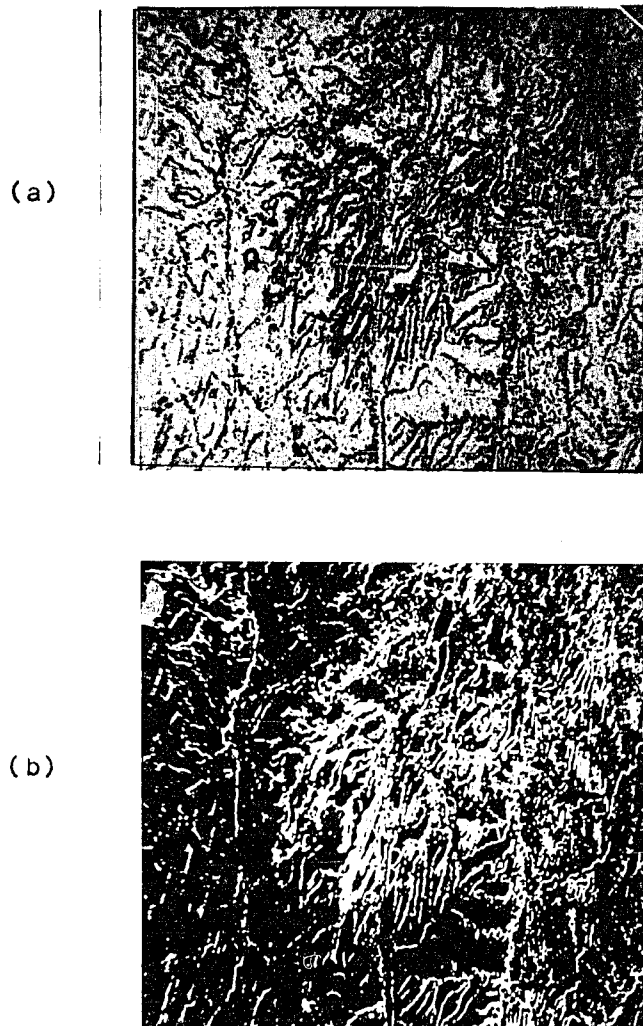


Figure 6.5. Co-occurrence matrix features. (a) Angular Second Moment (ASM) image. (b) Contrast (CON) image.

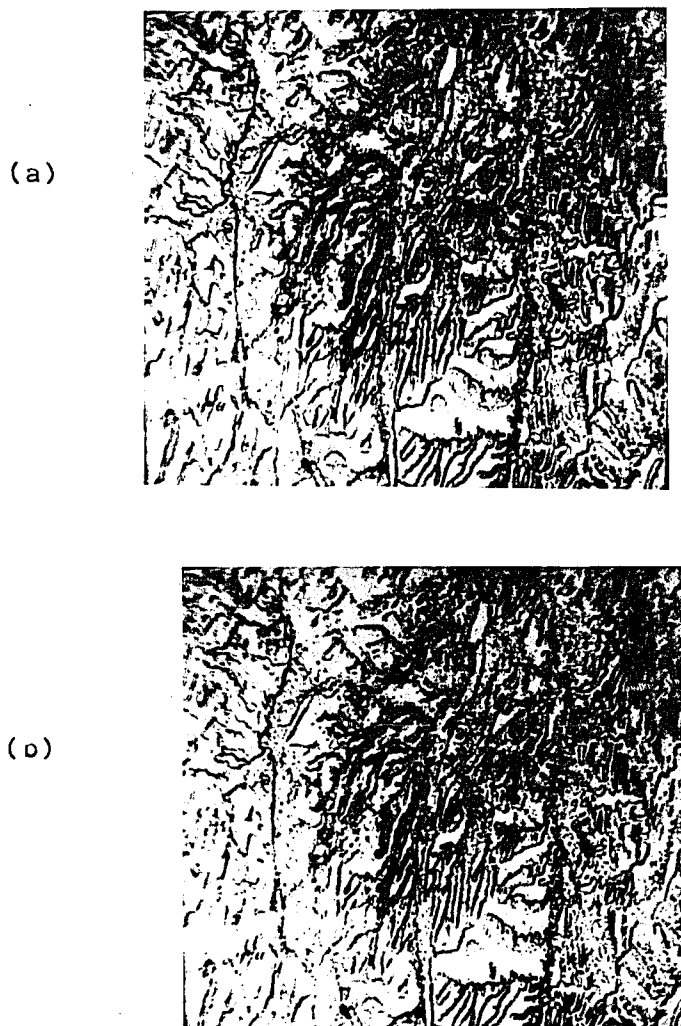


Figure 6.6. Textural transformation features. (a) Negatively transformed Standard Deviation image (STD) with a 3-by-3 window. (b) Negatively transformed Mean of Squared Length Differences image (MSQ) with a 3-by-3 window.



Figure 6.6. Textural transformation features. (c) Negatively transformed Range image (RAN) with a 3-by-3 window. (d) Negatively transformed Range image (RAN) with a 5-by-5 window.

(e)

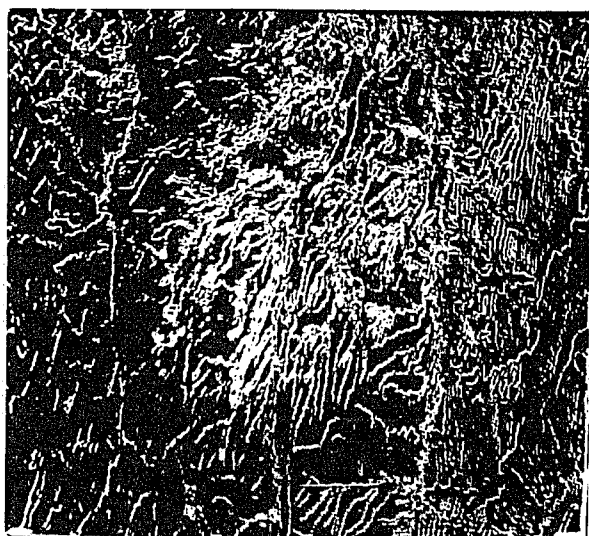


Figure 6.6. Textural transformation features. (e) A pseudocolored version of the Range image (RAN) with a 3-by-3 window.

CHAPTER 7

CONCLUSIONS

The objectives set forth for the image enhancement of the tonal and textural information have been met. The TMS imagery with high spatial, spectral, and radiometric resolution makes it possible to study the small local area by performing the principal components analysis and the texture analysis.

The principal components analysis is successful in the effort to compress image data by rearranging the total variance in the original data. It has the power in lithologic separations by maximizing minor but important tonal variations within the original data. The technique also has the ability to rank the signal to noise ratio. It provides the optimum representation of the data in single image format. Although PC2 and PC3 contain a small amount of total variance, they do show the superiority of the principal components analysis in lithologic separations which could not be easily observed in the unprocessed data. The improvements in lithologic separations are more apparent on the color-composites than they are on the individual component images. The result that allows the best visual discrimination of the lithologic units was

obtained by producing a color-composite from the first three components. The last comment on this technique is that the ratios of the original NS-001 data can be chosen to be the input data for the principal components analysis. Since shading influences resulting from low sun angle and rough topography in the original data is obvious, it could be a valuable preprocessing step to apply ratios suppressing topographic shading before application of principal components analysis to extract image tonal information. However, the shading influences are useful in the texture analysis because they can highlight geologic structures.

Principal component images are excellent for rock-type discrimination, but they are not so good for the visualization of faulted structures. Texture analysis results including gradient images, co-occurrence matrix and textural transformation features turned out to be very useful to extract textural information.

Gradient operators are a powerful tool for evaluating the local geologic structural trends in the study area. They could be regarded as a semi-automated mapping tool for lineaments.

Texture features, created from the co-occurrence matrices and textural transformation, are highly correlated either positively or negatively; they are numerically and

visually similar and provide similar textural information. The fact suggests that different texture extraction algorithms may have common intrinsic characteristics in describing textural information. The textural transformation, in this study, is more practical than the co-occurrence matrix algorithm from the computational point of view. The texture features derived from both algorithms work as edge detectors that automatically map textures which may reflect geologic structures, drainage density, or drainage patterns. The results provide a clearer view of textural information than gradient type images do. Although neither algorithm is sensitive enough to pick up subtle textural information that can be observed from the original data, the correlation between textures and geologic structures is high; some lineaments in the texture features could be used to interpret geologic structures. "Edge density" often reflects rock permeability, whereas drainage patterns represent lithologic characteristics of the underlying rocks or structural weakness. Both shown in the COM or textural transformation features aid lithologic interpretation in this study.

In addition, the texture features derived from the co-occurrence matrix and textural transformation provide additional information that can be gained by the qualitative analysis of the length, orientation, and

spatial distribution of the abundant short linear features presented in the texture features. They also provide a base image for a quantitative analysis of the linears; however, more advanced image processing techniques have to be developed for a quantitative analysis.

REFERENCES

- Abrams, M.J., Brown, D., Lepley, L., and Sadowski, R., 1983, Remote sensing for porphyry copper deposits in Southern Arizona: *Economic Geology*, Vol. 78, No. 4, pp. 591-604.
- Bailey, G.B., Francica, J.R., Dwyer, J.L., and Feng, M.S., 1982, Extraction of geologic information from Landsat Multispectral scanner and Thematic Mapper Simulator data from the Uinta and Piceance Basins, Utah and Colorado: *International Symposium on Remote Sensing of Environment, Second Thematic Conference, Remote Sensing for Exploration Geology*, Fort Worth, Texas, December 6-10.
- Ballard, D.H., and Brown, C.M., 1982, Computer Vision, Prentice-Hall Inc., Englewood Cliffs, New Jersey, 513p.
- Drewes, H., 1972a, Structural geology of the Santa Rita Mountains southeast of Tucson, Arizona: *U. S. Geol. Survey Prof. Paper 748*, 35p.
- Drewes, H., 1972b, Cenozoic rocks of the Santa Rita Mountains southeast of Tucson, Arizona: *U.S. Geol. Survey Prof. Paper 746*, 66p.
- Fontanel, A., Blanchet, C., and Lallemand, C., 1975, Enhancement of Landsat imagery by combination of multispectral classification and principal component analysis: *Proc. of the NASA Earth Resources Survey Symposium*, Vol. I-B, pp. 991-1012.
- Gonzalez, R.C., and Wintz, P., 1977, Digital Image Processing, Addison-Wesley, Reading, MA.
- Haralick, R.M., Shanmugam, K., and Dinstein, I., 1973, Textural features for image classification: *IEEE Transactions on Systems, Man and Cybernetics*, Vol. SMC-3, No. 6, pp. 610-621.
- Haralick, R.M., 1979, Statistical and structural approaches to texture: *Proceedings of the IEEE*, Vol. 67, No. 5, pp. 768-804.

- Irons, J.R., and Petersen, G.W., 1981, Texture transforms of remote sensing data: Remote Sensing of Environment, Vol. 11, pp. 359-370.
- Jensen, J.R., 1979, Spectral and textural features to classify elusive land cover at the urban fringe: Professional Geographer, Vol. 31, No. 4, pp. 400-409.
- Jenson, S.K., and Waltz, F.A., 1979, Principal components analysis and canonical analysis in remote sensing: Proc. Am. Soc. Photogr. 45th Ann. Meeting, pp. 337-348.
- Julesz, B., 1962, Visual pattern discrimination: IRE Trans. Inform. Theory, Vol. 8, No. 2, pp. 84-92.
- Kahle, A.B., Madura, D.P., and Soha, J.M., 1980, Middle infrared multispectral aircraft scanner data: analysis for geologic applications: Applied Optics, Vol. 19, pp. 2279-2290?.
- McNew, G.E., 1981, Tactite alteration and its late stage replacement in the southern half of the Rosemont mining district, Arizona: Unpublished M.S. Thesis, University of Arizona, Tucson, 70p.
- Podwysocki, M.H., Moik, J.G., and Shoup, W.C., 1975, Quantification of geologic lineaments by manual and machine processing techniques: Proc. of the NASA Earth Resources Survey Symposium Vol. I-B, pp. 885-903.
- Popoff, C., 1940, The geology of the Rosemont mining camp, Pima County, Arizona: Unpublished M.S. thesis, The University of Arizona, Tucson, 109p.
- Richards, J.A., 1984, Thematic mapping from multispectral image data using the principal components transformation: Remote Sensing of Environment, Vol. 16, pp. 35-46.
- Rosenfeld, A. and Troy, E., 1970, Visual texture analysis: Tech. Rep. 70-116, University of Maryland, College Park, MD.
- Sadowski, R.M., and Abrams, M.J., 1982, Mapping hydrothermal alteration using aircraft VNIR scanner at the Rosemont porphyry copper deposit: 2nd Them. Conf., Intl. Symp. on Remote Sensing of Envir., Fort Worth, TX, V.2, pp. 175-188.

- Santisteban, A., and Munoz, L., 1977, Application of image principal component technique to the geologic study of a structural basin in central Spain: Machine Processing of Remotely Sensed Data Symposium, pp. 228-236.
- Schowengerdt, R.A. 1981, Texture feature extraction: Final report on USGS Grant # 14-03-00001-G-664.
- Schowengerdt, R.A., 1983, Techniques for Image Processing and Classification in Remote Sensing, Academic Press, New York, NY, 249p.
- Siegal, B.S., and Gillespie, A.R., 1980, Remote Sensing in Geology, John Wiley & Sons, New York, 702p.